Journal of Asian Earth Sciences 88 (2014) 85–97

Contents lists available at ScienceDirect

Journal of Asian Earth Sciences

journal homepage: www.elsevier.com/locate/jseaes

Chronology, geochemistry and Sr–Nd isotope studies of Jurassic intrusions in the Diyanqinamu porphyry Mo mine, central Inner Mongolia, China

Hairui Sun [a,b], Zhilong Huang [a,*], Wenbo Li [c], Chengbiao Leng [a], Deyun Ma [d], Xingchun Zhang [a]

[a] State Key Laboratory of Ore Deposit Geochemistry, Institute of Geochemistry, Chinese Academy of Sciences, Guiyang 550002, China
[b] University of Chinese Academy of Sciences, Beijing 100049, China
[c] The Key Laboratory of Orogenic Belts and Crustal Evolution, School of Earth and Space Sciences, Peking University, Beijing 100871, China
[d] Shandong Goldgroup Co., Ltd., Jinan 250014, China

ARTICLE INFO

Article history:
Received 17 September 2013
Received in revised form 6 March 2014
Accepted 18 March 2014
Available online 25 March 2014

Keywords:
Porphyry Mo
Jurassic granite
Diyanqinamu
Great Xing'an Range
Mongol-Okhotsk Orogenic belt
Central Asian Orogenic Belt

ABSTRACT

Available cores of porphyritic granite and aplitic granite from the Diyanqinamu porphyry Mo deposit in the north central Great Xing'an Range presented an opportunity to examine and analyze Mesozoic igneous rocks far from the Paleo-Pacific subduction zone. The Diyanqinamu granites are highly fractionated I-type, distinguished from the M-, A- or S-type granite by: high SiO_2, and Rb; low Zr, Nb, Y, and Ce; low $Fe_2O_3^{total}$/MgO and $(K_2O + Na_2O)$/CaO ratios; low alumina saturation index (<1.1); low initial I_{Sr} ratios (0.70137–0.70451); positive $\varepsilon Nd(t)$ values (2.37–3.77); and negative correlation between P_2O_5 and SiO_2. The aplitic granites were generated by fractional crystallization of the porphyritic granite, as evidenced by: spatial proximity; consistent zircon U–Pb ages (156 Ma) within error; correlations between other oxides and SiO_2 in Haker diagrams; low Ba, Sr, Nb, P, Ti, Eu; linear relationship in both $(La/Yb)_N$ vs. La and Sr vs. Ba diagrams; and, decreasing LREE and $\sum$REE with increasing SiO_2. The Diyanqinamu granites have young depleted-mantle two-stage model ages (avg. T_{DM2} = 660 Ma) similar to those of most Mesozoic voluminous felsic magmas in northeastern China, and were likely sourced from pre-existent crustal components both "old" and juvenile that had been juxtaposed during the tectonic evolution of the Paleo-Asian Ocean. These granites project in the transitional field from syn-collision to post-collision tectonic settings on tectonic discrimination diagrams, implying emplacement in an extensional environment. Extensional volcanism and basin formation in the Great Xing'an Range region in Late Jurassic is coeval with the Diyanqinamu granites, demonstrating that post-orogenic lithospheric extension related to the closure of the Mongol-Okhotsk Ocean was the main driving force for Late Jurassic magmatism in this region.

1. Introduction

Late Mesozoic igneous rocks are widely exposed in the Great Xing'an Range, and recently have been the focus of much study (Gou et al., 2013; Guo et al., 2010; Xu et al., 2013; Ying et al., 2010; Zhang et al., 2008a,b, 2010, 2011b; Zhao et al., 2013). Several models have been postulated to account for petrogenesis of these rocks, though none of the models is yet widely accepted, including: a mantle plume (Ge et al., 1999; Lin et al., 1999); subduction of the Paleo-Pacific plate and related processes (Jiang and Quan, 1988; Zhang et al., 2010); and, closure of the Mongol-Okhotsk Ocean (Fan et al., 2003; Meng, 2003). The studies on which these models are based were mainly focused on the northern Great Xing'an Range, where various geodynamic fields were superposed during the Late Mesozoic. Intermingling of tectonic signatures of the closure of the Mongol-Okhotsk Ocean and the subduction of the Paleo-Pacific plate has caused significant difficulty in interpretation of the different tectonic products of this dynamism. Studies of the central Great Xing'an Range remain relatively scarce, even though the central part of the range is far from the subduction belt of the Pacific plate. For this study, we focused on intrusions within the central part of the range, to understand the genetic mechanism of Late Mesozoic magmatism in the absence of the complications of Pacific plate subduction. We anticipated that our study area would be primarily representative of the spatial and temporal influence of the Mongol-Okhotsk tectonic regime.

* Corresponding author. Tel.: +86 851 5895900; fax: +86 851 5891664.
E-mail address: huangzhilong@vip.gyig.ac.cn (Z. Huang).

http://dx.doi.org/10.1016/j.jseaes.2014.03.014
1367-9120/

Specifically, we were able to study granites in drill cores at the Diyanqinamu porphyritic molybdenum deposit, located in the north central Great Xing'an Range (Fig. 1b) and formed in the Late Jurassic (Leng et al., unpublished data). Diyanqinamu is a recently discovered large-scale porphyry Mo resource with a reserve of at least 0.79 Mt of molybdenum metal at an average grade of 0.099% (Fig. 2). We present here the first detailed study of the ore-forming related intrusions in this mine, including: zircon U–Pb ages, major elements, trace elements, and whole rock Sr–Nd isotopes. Available core samples provided a unique opportunity to study the genesis of these granites and further decipher the tectonic mechanisms of this region during the Late Mesozoic.

2. Regional geology

The Great Xing'an Range is part of the eastern segment of the Central Asian Orogenic Belt (CAOB) (Jahn et al., 2000), also known as the Altaid Tectonic Collage (Sengör et al., 1993). The CAOB mainly formed by progressive subduction of the Paleo-Asian Ocean and amalgamation of terranes of different types and derivation in the Paleozoic (Jahn et al., 2000, 2004; Wu et al., 2000). The CAOB is characterized by the presence of significant juvenile crust, with widespread Paleozoic and Mesozoic granites exhibiting positive $\varepsilon Nd(t)$ and young Nd model ages (Hong et al., 2000, 2003; Jahn et al., 2000, 2001, 2004; Wu et al., 2000, 2002, 2011).

The Paleozoic configuration of the Great Xing'an Range was overprinted by events in the Late Mesozoic, including creation both of the Mongol-Okhotsk Ocean tectonic domain (Liu et al., 2011) and of the Circum-Pacific Ocean tectonic domain (Nie et al., 2010). The Mongol-Okhotsk domain in the northern Great Xing'an Range marks the suture between the Siberian and North China cratons (Sengör and Natal'in, 1996), formed by the closure of the Mongol-Okhotsk Ocean beginning in the Triassic (Zonenshain et al., 1990). Metelkin et al. (2007, 2010) and Tomurtogoo et al. (2005) suggested that closure of the Mongol-Okhotsk Ocean, which proceeded in a scissor-like fashion from west to east, was completed in eastern Mongolia and Siberia in Jurassic–early Cretaceous. The eastern Mongol-Okhotsk domain is characterized by Early Jurassic calc-alkaline volcanic rocks and porphyry Cu–Mo ore deposits within the Erguna Massif (Wu et al., 2001).

During the Late Mesozoic, the Mongol-Okhotsk tectonic regime was in part overprinted by the Paleo-Pacific tectonic regime (Xu et al., 2013), controlled by the subduction of the Paleo-Pacific plate underneath Eurasia (Maruyama and Send, 1986). This subduction was accompanied by voluminous igneous rocks (Wu et al., 2005; Zhang et al., 2008a,b, 2011b), widespread rifting (Ren et al., 2002), and the accretion of the Circum-Pacific orogenic belt (Isozaki et al., 2010; Utsunomiya et al., 2008; Wu et al., 2007; Zhou et al., 2009).

In Diyanqinamu and adjacent areas, the basement lithology is discontinuously exposed and mainly consists of strata of

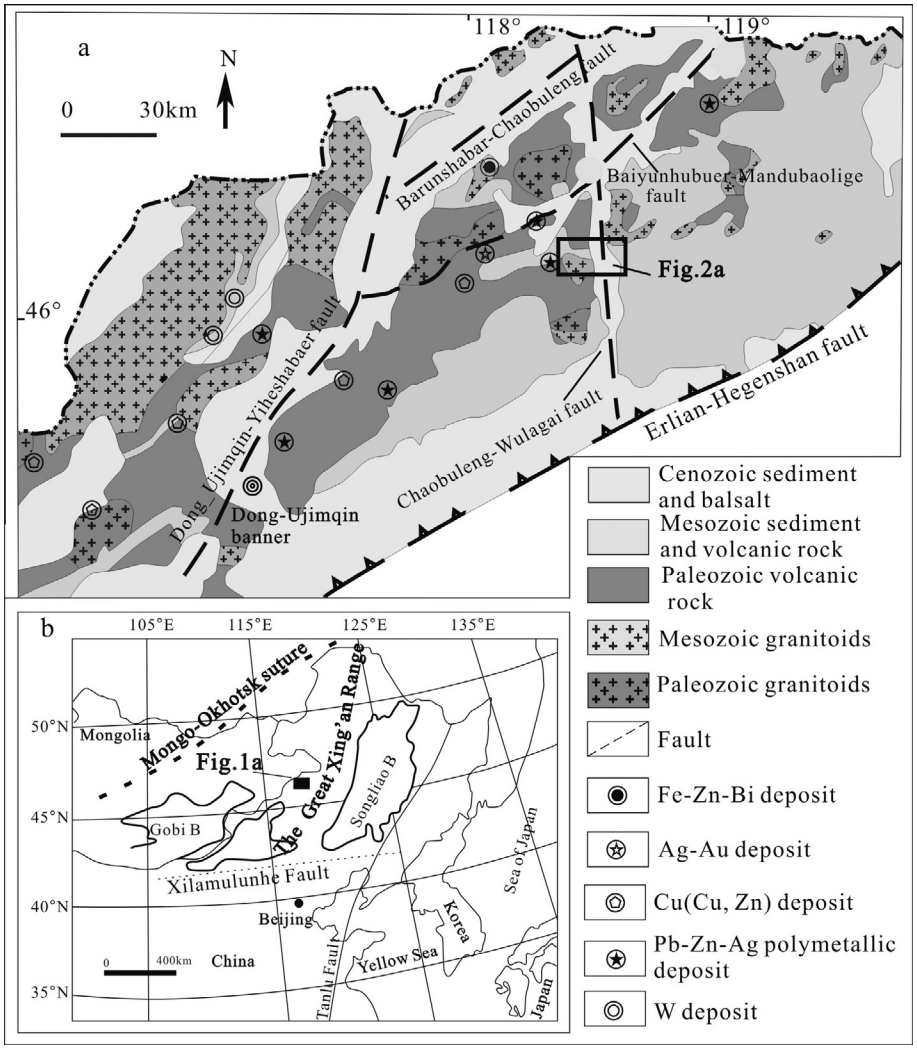

Fig. 1. Simplified geological map (a), and tectonic map (b), of the Diyanqinamu Mo deposit and adjacent areas (Zhang et al., 2008b; Zhang, 2008).

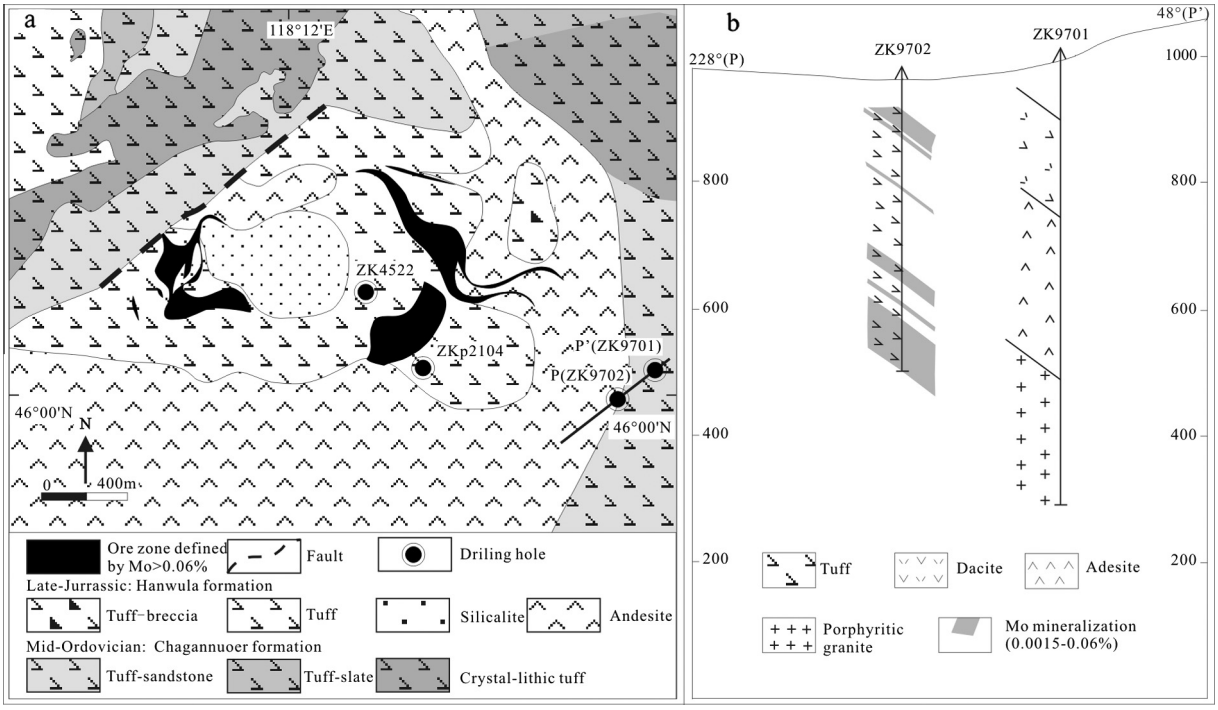

Fig. 2. Simplified geologic map of the Diyanqinamu porphyry Mo deposit (a), and profile from location P to P′ (b).

Ordovician, Silurian, Carboniferous, and Jurassic ages (Zhang et al., 2008c); Precambrian blocks are absent (Xue et al., 2009). Magmatism was pervasive in the region from Paleozoic through Mesozoic time (Fig. 1a), and a particularly active period of magmatism during the Late Paleozoic and Early Mesozoic is closely related to various economic mineral resources (Hong et al., 2003; Nie et al., 2004; Zhang et al., 2008c; Zhang, 2008). The intrusive bodies at Diyanqinamu are porphyritic granite, discovered in the drill hole ZK9701, and aplitic granites penetrated in drill holes ZK4522 and ZKp2104 (Fig. 2). The granites are located in the southeast quadrant of the Diyanqinamu mine, intruded into Jurassic strata (Fig. 2b). The contact relationship among the granites is poorly constrained because they do not crop out and there are only the three drill hole penetrations.

3. Petrography

The aplitic granite intercepts in drill holes ZK4522 and ZKp2104 are about 400 m apart (Fig. 2a). These granites both show aplitic texture in hand samples and porphyritic texture in thin sections, with minor volume percent of phenocrysts compared with that of the porphyritic granite. Both aplitic granites are similar in composition and contain a few potassium feldspar phenocrysts (Fig. 3e and i), though the potassium feldspar was widely altered into sericite or clay minerals (Fig. 3f).

The aplitic granite in ZK4522 was more intensively altered than that in ZKp2104. The ZK4522 granite was impacted by large-scale silicification in a stockwork of quartz (Fig. 3g) and cemented by quartz veins, resembling "phenocrysts" of typical porphyry. Of particular interest, a unidirectional solidification texture (UST, Fig. 3h) is observed in drill hole ZK4522 at the apex of the aplitic granite. This UST establishes a framework for the magmatic event and for hydrothermal activity, particularly for the widely scattered silicification of quartz veins overlying the aplitic granite. Based on their close spatial relationship and their similar mineral compositions, the aplitic granites drilled in ZK4522 and ZKp2104 are probably the same intrusive body, connected at depth.

The porphyritic granite in drill hole ZK9701 occurs at >504 m in depth. The phenocrysts comprise quartz (ca. 30%), potassium feldspar (ca. 35%), plagioclase (ca. 27%) and biotite (ca. 5%), with minor amounts of magnetite, zircon, and apatite (Fig. 3a–c). Plagioclase displaying polysynthetic twinning was altered to sericite, clay minerals, or chlorite and epidote (Fig. 3c). Potassium feldspar displaying Carlsbad twinning was extensively altered to clay minerals (Fig. 3b). Biotite demonstrating schistose texture was altered only locally. Quatrz, one of the dominant minerals, is rounded in shape, displaying obvious corrosion texture (Fig. 3c).

4. Sampling and analytical methods

Eleven samples of igneous rock were collected from drilling holes ZK9701 and ZKp2104. All of them were pulverized into granules smaller than 200 mesh in agate mortars to minimize potential contamination and were then analyzed for major element compositions of minerals, trace element abundances, and isotopic analyses. Major oxides were analyzed by X-ray fluorescence spectrometry (XRF) at the ALS Laboratory Group of Guangzhou, China. The analytical errors for major oxides were generally less than ±2%. Trace element and rare earth element abundances were determined using a PE Elan 6000 ICP-MS at the State Key Laboratory of Ore Deposit Geochemistry, Institute of Geochemistry, Chinese Academy of Sciences (IGCAS). The powdered samples (50 mg) were dissolved in high-pressure Teflon bombs using a $HF + HNO_3$ mixture for 48 h at ≈190 °C (Qi and Grégoire, 2000). Rh was used as an internal standard to monitor signal drift during counting. The international standards GBPG-1 and OU-6 and the Chinese National standards GSR-1 and GSR-3 were used for analytical quality control. The analytical precision was generally better than 5% for trace elements.

Sr and Nd isotopic measurements were conducted on thermal ionization mass spectrometry (TIMS) at the State Key Laboratory of Ore Deposit Geochemistry, Institute of Geochemistry, Chinese Academy of Sciences, Guiyang. The analytical procedures for both Sr and Nd isotopic determinations were similar. Samples were

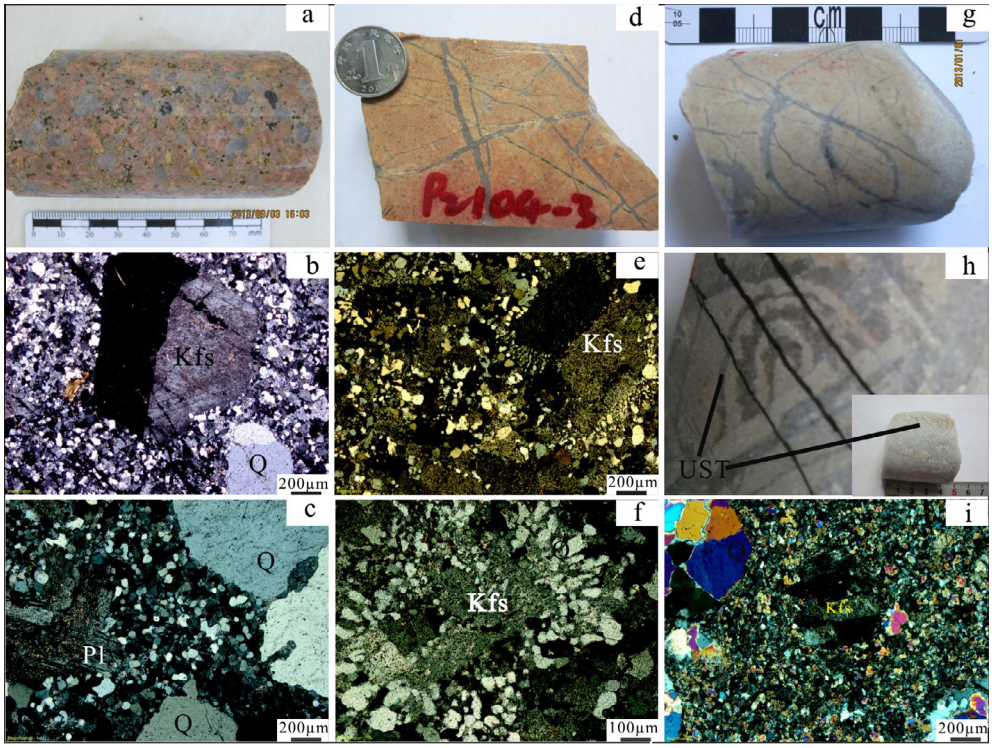

Fig. 3. Photographs and photomicrographs of granites from the Diyanqinamu mine. Porphyritic granite: (a) altered porphyritic granite, (b) Carlsbad twin of potassium feldspar phenocryst, (c) sericitization alteration of plagioclase phenocryst. Aplitic granite in drill hole ZKp2104: (d) silicification of aplitic granite, (e) Carlsbad twin of potassium feldspar phenocryst, (f) potassium phenocryst altered by sericitization. Aplitic granite in drill hole ZK4522: (g) silicification of aplitic granite, (h) unidirectional solidification texture (UST) in aplitic granite, (i) Carlsbad twin of potassium feldspar phenocryst.

dissolved in HF + $HClO_4$. Rb, Sr, and REE were separated using AGW50 × 12 cation exchange columns. The REE were further dissolved in 0.1 N HCl, then Sm and Nd were separated on the levextrel resin ion exchange columns. $^{87}Rb/^{86}Sr$ and $^{147}Sm/^{144}Nd$ ratios analyzed at the Institute of Geochemistry were calculated using the Rb, Sr, Sm, and Nd abundances measured by ICP-MS. Several analyses on the NBS-987 Sr standard yielded $^{87}Sr/^{86}Sr = 0.710254 \pm 5$ (2σ). The mean $^{143}Nd/^{144}Nd$ ratios for the La Jolla and Jndi-1 Nd standard were 0.511544 ± 3 (2σ) and 0.512104 ± 5 (2σ) respectively. $^{143}Nd/^{144}Nd$ ratios were normalized to the value of $^{146}Nd/^{144}Nd = 0.7219$. Fractionation effects during the Sr isotopic composition runs were eliminated by normalizing to an $^{86}Sr/^{88}Sr$ value of 0.1194.

Zircon grains were separated from porphyritic granite and aplitic granite in this mine. The zircon grains were then mounted in epoxy resin and polished to approximately half of their thickness. Examination of the internal structure was performed using a Cathode Luminescence imaging technique with a scanning electron microscope (SEM) JSM6510 from Japan. The zircons characterized by the absence of oscillating zones and intensive hydrothermal alteration were avoided in these analyses. A U–Pb geochronology of zircon was conducted by LA-ICP-MS at the State Key Laboratory of Ore Deposit Geochemistry, Institute of Geochemistry, Chinese Academy of Sciences, Guiyang. A GeoLasPro laser-ablation system (Lamda Physik, Gottingen, Germany) and an Agilent 7700x ICP-MS (Agilent Technologies, Tokyo, Japan) were combined for the experiments. The 193 nm ArF excimer laser, homogenized by a set of beam delivery systems, was focused on the zircon surface with a fluence of 10 J/cm^2. According to the grain size of the zircon, the ablation protocol employed spot diameters of 44 and 32 μm at 3 Hz and 5 Hz repetition rates for 40 s (equating to 120 and 200 pulses) for zircons from porphyry and aplite respectively. Helium was applied as a carrier gas to efficiently transport aerosols to the ICP-MS. Zircon 91500 was used as an external standard to correct instrumental mass discrimination and elemental fractionation. Zircon GJ-1 and Plešovice were treated as quality controls for the geochronology analysis. The lead abundance of zircon was externally calibrated against the NIST SRM 610 using Si as internal standard, whereas Zr was used as an internal standard for the other trace elements (Hu et al., 2011; Liu et al., 2010a). Raw data calculation was performed off-line by ICPMSDataCal software (Liu et al., 2010a, 2010b).

5. Results

5.1. Major and trace element composition

Analyses of 11 granitic samples from drill holes ZKp2104 (aplitic) and ZK9701 (porphyritic) are listed in Table 1. Although there are slight differences in SiO_2, Al_2O_3, and CaO, most of these samples have similar results for major elements. Table 1 shows that most of the samples are silica-rich (avg. 73.93 wt% SiO_2) but low in Ca (avg. 0.70 wt% CaO), Mg (avg. 0.26 wt% MgO), Mn (avg. 0.07 wt% MnO), Ti (avg. 0.17 wt% TiO), Fe (avg. 1.2 wt% $Fe_2O_3^{tal}$), and P (avg. 0.04 wt% P_2O_5), except that sample ZK9701-21 has low SiO_2 (67.86 wt%). All of these granites are moderately- to slightly peraluminous, as indicated by the presence of normative corundum (Table 1 and Fig. 4b), and belong to the high-K calc-alkaline series (Fig. 4a), with high K_2O (avg. 4.91 wt%) compared with Na_2O. Harker diagrams show that the porphyritic and aplitic granites are chemically correlatable (Fig. 5).

The porphyry and aplite granites share similar characteristics in rare earth elements (REE) and trace elements. Both have high ratios of light to heavy REE, high $(La/Yb)_N$ ratios, and significant negative Eu anomalies, suggesting enrichment in light REE (LREE) and depletion in heavy REE (HREE; Table 1 and Fig. 6a). ∑REE shows negative correlation with increasing SiO_2 from porphyritic granite to aplitic granite, while HREE displays positive correlation (Table 1

Table 1
Major (wt%), rare earth and trace element (ppm) data for granities in Diyanqinamu Mo deposit.

	Aplitic grantie ZKp2104				Porphyritic grantie ZK9701						
Sample no.	-2	-3	-4	-5	-16	-17	-18	-19	-20	-21	-22
Analyte (wt%)											
SiO_2	76.59	75.9	75.44	75.37	73.67	73.21	73.45	74.4	72.05	67.86	75.33
TiO_2	0.07	0.07	0.06	0.06	0.19	0.19	0.19	0.19	0.28	0.44	0.15
Al_2O_3	11.5	12.11	11.68	11.68	12.8	13.07	12.98	12.5	13.45	14.96	11.94
Fe_2O_3	0.73	0.59	0.98	0.8	0.6	0.62	0.66	0.59	0.93	1.27	1.03
FeO	0.26	0.32	0.19	0.26	0.52	0.58	0.52	0.58	0.64	0.9	0.26
MnO	0.07	0.03	0.1	0.06	0.06	0.06	0.06	0.06	0.11	0.1	0.06
MgO	0.18	0.16	0.26	0.15	0.25	0.28	0.25	0.24	0.38	0.55	0.18
CaO	0.43	0.35	0.69	0.60	0.66	0.77	0.84	0.57	1.06	1.20	0.50
Na_2O	2.8	2.93	2.67	2.75	3.32	3.47	3.18	2.96	3.41	4.01	2.7
K_2O	5.01	5.06	4.52	5.17	4.96	4.67	5.14	5.07	4.81	4.6	4.99
P_2O_5	0.01	<0.01	<0.0	<0.0	0.04	0.05	0.05	0.04	0.07	0.11	0.02
LOI	1.59	1.7	2.07	1.7	1.77	1.97	1.72	1.63	2.18	2.37	1.86
Total	99.24	99.23	98.66	98.6	98.85	98.93	99.04	98.82	99.36	98.37	99.03
$Fe_2O_3^{total}$	1.02	0.95	1.19	1.09	1.18	1.26	1.24	1.23	1.64	2.27	1.32
A/CNK	1.06	1.11	1.11	1.04	1.06	1.07	1.05	1.1	1.05	1.09	1.11
Cm	0.72	1.21	1.19	0.49	0.9	1.05	0.79	1.23	0.89	1.52	1.28
DI	95.29	95.38	92.95	94.62	93.69	92.8	92.83	93.76	90.74	88.26	94.04
Trace (ppm)											
Rb	226	217	241	247	245	259	266	245	277	269	324
Sr	83.8	64.6	58.4	79.7	65	69.2	76.5	60.7	100	158	37.8
Ba	205	128	187	181	231	256	273	244	315	704	144
Zr	110	103	105	118	139	133	136	139	196	337	117
Hf	6.50	6.33	6.20	7.34	5.47	5.06	5.33	6.04	6.41	7.97	5.00
Nb	20.5	27.0	27.0	30.8	22.4	19.7	20.6	22.8	19.1	16.6	20.6
Ta	2.44	2.49	2.6	3.14	2.10	1.89	1.92	2.29	1.73	1.18	2.26
Mo	19.7	13.1	10.6	9.51	3.27	1.12	3.02	1.60	6.98	2.73	2.04
Cs	4.10	4.21	5.54	3.99	6.68	8.30	8.00	7.59	8.71	10.17	7.49
La	13.1	20.2	25.3	18.7	43.7	42.9	35.3	45.3	38.9	36.4	44.8
Ce	23.3	33.9	41.8	32.4	74.3	70.8	60.3	74.0	72.0	70.2	69.3
Pr	2.14	2.85	3.6	2.78	7.48	6.98	6.10	6.80	7.47	7.87	6.18
Nd	5.97	7.37	9.56	7.66	22.6	21.6	19.0	20.2	23.5	26.8	17.5
Sm	0.960	1.10	1.50	1.20	3.78	3.67	3.08	3.37	3.95	4.74	2.84
Eu	0.24	0.14	0.25	0.18	0.51	0.56	0.48	0.46	0.65	0.96	0.35
Gd	0.85	0.95	1.10	0.94	2.49	2.57	2.07	2.2	2.47	2.83	1.86
Tb	0.16	0.17	0.24	0.22	0.48	0.45	0.41	0.4	0.48	0.52	0.35
Dy	1.05	1.14	1.58	1.45	2.55	2.43	2.38	2.21	2.6	2.62	1.94
Ho	0.3	0.31	0.4	0.4	0.59	0.57	0.56	0.53	0.58	0.58	0.44
Er	1.00	1.20	1.44	1.36	1.99	1.92	1.78	1.80	1.92	1.82	1.51
Tm	0.19	0.23	0.26	0.27	0.32	0.31	0.27	0.29	0.29	0.26	0.22
Yb	1.46	1.86	2.13	2.24	2.38	2.25	2.05	2.23	2.11	1.97	1.82
Lu	0.24	0.33	0.37	0.39	0.4	0.4	0.36	0.4	0.35	0.3	0.32
Y	9.16	10.83	13.7	11.3	18.7	18.0	16.8	16.8	17.5	16.6	14.0
Ga	16.5	17.3	18.7	18.7	19.4	19.8	18.9	18.8	19.9	20.7	17.4
Pb	78.6	58.8	162	116	33.1	29.6	35.2	33.3	35.5	34.8	83.4
Th	41.6	43.2	44.2	58.0	33.8	35.4	34.6	39.9	29.2	17.0	42.2
U	11.3	14.6	13.6	16.4	13.0	10.7	10.6	16.1	8.3	5.19	10.2
ΣREE	50.96	71.73	89.58	70.23	163.54	157.37	134.11	160.26	157.18	157.79	149.44
LREE/HREE	8.72	10.59	10.89	8.68	13.61	13.43	12.57	14.93	13.57	13.47	16.64
La_N/Yb_N	6.43	7.79	8.51	6	13.2	13.68	12.35	14.56	13.25	13.23	17.66
δEu	0.78	0.41	0.58	0.5	0.48	0.53	0.54	0.49	0.59	0.74	0.44
Rb/Sr	2.69	3.36	4.13	3.09	3.77	3.74	3.47	4.03	2.77	1.7	8.59
Nb/Ta	8.42	10.86	10.41	9.81	10.65	10.42	10.72	9.96	11.04	13.99	9.12
La/Yb	8.96	10.86	11.86	8.36	18.4	19.07	17.21	20.29	18.47	18.45	24.62

DI means differentiation index; Cm is the abbreviation of corundum; ACNK = $(Al_2O_3)/(K_2O + Na_2O + CaO)$ molar ratio. ANK = $(Al_2O_3)/(K_2O + Na_2O)$ molar ratio.

and Fig. 6a). In a primitive mantle-normalized plot, they are enriched in large-ion lithophile elements (LILE) such as Rb, K, U, Th, and LREE, and are depleted in high field strength elements (HFSE) such as Nb, Ta, Ti, and P (Fig. 6b).

5.2. Sr–Nd isotopic composition

Isotopic results for Rb–Sr and Sm–Nd (Table 2). The aplitic granite has positive $\varepsilon Nd(t)$ values from 3.3 to 3.8, homogeneous $(^{143}Nd/^{144}Nd)_i$ ratios from 0.51256 to 0.51260, and heterogeneous initial $(^{87}Sr/^{86}Sr)_i$ ratios from 0.7014 to 0.7021 (Table 2). Similarly, the porphyritic granite samples also have positive $\varepsilon Nd(t)$ values from 2.6 to 3.2, homogeneous $(^{143}Nd/^{144}Nd)_i$ ratios from 0.51261 to 0.51263, and heterogeneous initial $(^{87}Sr/^{86}Sr)_i$ from 0.7026 to 0.7045 (Table 2). The heterogeneity of initial $(^{87}Sr/^{86}Sr)_i$ ratios for these granites may be due to hydrothermal alteration. Based on the model of Liew and Hofmann (1988), the two-stage Nd model age for the aplitic granite is 0.66–0.72 Ga and that of porphyritic granite is 0.62–0.65 Ga.

5.3. Zircon U–Pb age

Zircons from both the porphyritic and the aplitic granites have clear oscillating zones (Fig. 7a and c), indicating magmatic origin. Results of the zircon LA-ICP-MS analyses are listed in Table 3, and the errors of weighted mean ages are 1σ.

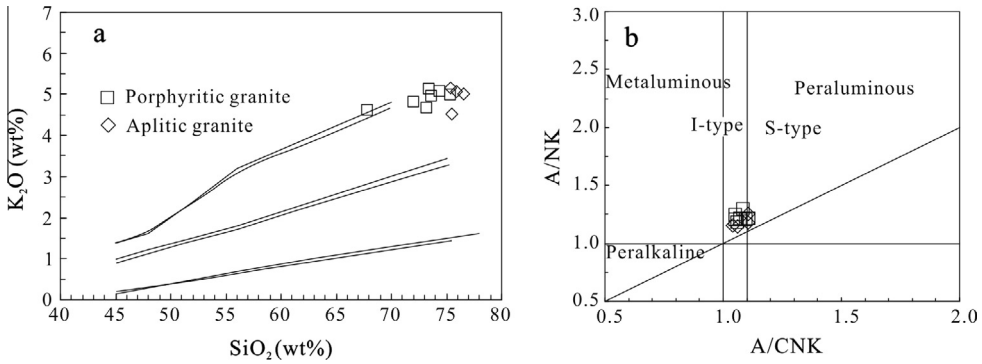

Fig. 4. SiO_2–K_2O plot (a) and Al/[Ca + Na + K] (molar) vs. Al/[Na + K] (molar) plot (b) of the granites in the Diyanqinamu granites.

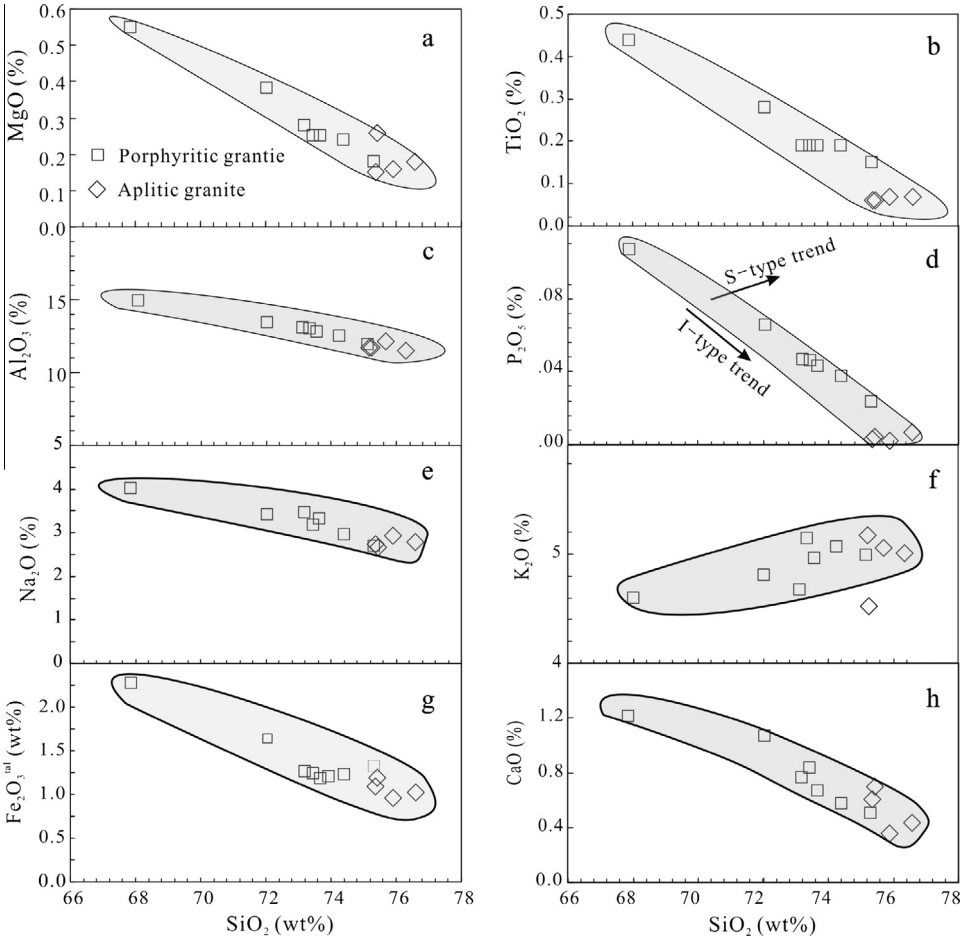

Fig. 5. Harker variation diagrams for the porphyritic granite and aplitic granite in the Diyanqinamu mine.

Zircon grains from porphyritic granite in drill hole ZK9701 have U and Th contents of 159–990 ppm and 109 to 492 ppm respectively, with Th/U ratios of 0.49–1.15 (Table 3), indicating a magmatic origin. LA-ICP-MS U–Pb results are shown in Fig. 7b and display a narrow range of ratios, with a weighted mean $^{206}Pb/^{238}U$ age of 156 ± 1 Ma (MSWD = 0.90), representing the emplaced age of this granite.

Zircon grains from aplitic granites in drill hole ZK4522 have U contents of 550–1143 ppm (avg. 844 ppm), Th contents of 400–1647 ppm (avg. 857 ppm), and Th/U ratios from 0.73 to 1.44 (Table 3), indicating that they are of magmatic origin as well. Fig. 7d shows weighted mean $^{206}Pb/^{238}U$ age of 156 ± 1 Ma (MSWD = 0.41), reflecting the crystallization age of the aplitic granite, which is indistinguishable from the porphyritic granite within error.

6. Discussion

6.1. Genetic type of the granites

Petrogenesis of granitic rocks has a clear bearing on models of tectonic setting (Sylvester, 1989; Whalen et al., 1987), and the correct classification of felsic granites is particularly important. Granitic rocks have been divided into I-, S-, M-, and A-types according to their protolithic nature (Pitcher, 1982, 1993; Xu et al., 2007). According to the discrimination criteria proposed by

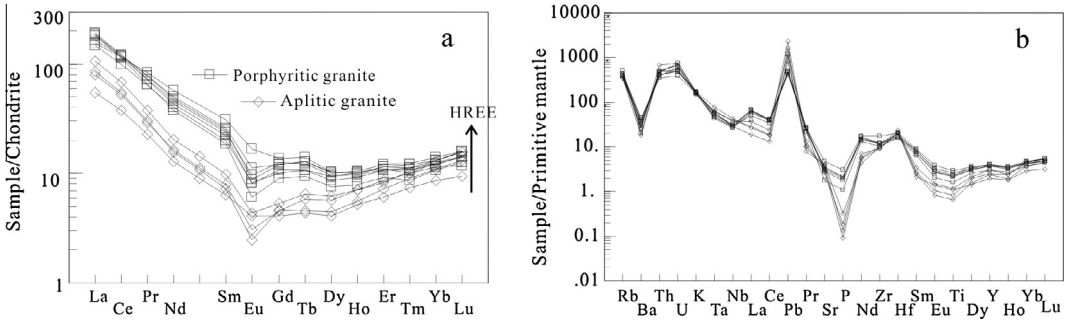

Fig. 6. Chondrite-normalized REE distribution diagram (a), and primitive mantle-normalized trace element spider diagram of the granites (b), in the Diyanqinamu (referenced values from Sun and McDonough (1989)).

Table 2
Sr–Nd isotopic data for the granites in Diyanqinamu Mo deposit.

Lithology	Aplitic grantie ZKp2104				Porphyritic granite ZK9701				
Sample no.	-2	-3	-4	-5	-16	-17	-18	-20	-21
t (Ma)	156	156	156	156	156	156	156	156	156
Rb (ppm)	226	217	241	247	245	259	266	277	269
Sr (ppm)	83.8	64.7	58.4	79.7	65.0	69.2	76.5	60.7	100
$^{87}Rb/^{86}Sr$	7.797	9.730	11.96	8.954	10.90	10.83	10.05	8.007	4.915
$^{87}Sr/^{86}Sr$	0.718661	0.723698	0.728055	0.721807	0.727691	0.728214	0.724885	0.722037	0.715411
2σ	16	10	10	10	12	8	16	12	16
$(^{87}Sr/^{86}Sr)_i$	0.7014	0.7021	0.7015	0.7020	0.7035	0.7042	0.7026	0.7043	0.7045
Sm (ppm)	0.96	1.10	1.50	1.20	3.78	3.67	3.08	3.95	4.74
Nd (ppm)	5.97	7.37	9.56	7.66	22.6	21.6	19.0	23.5	26.8
$^{147}Sm/^{144}Nd$	0.0970	0.0899	0.0946	0.0942	0.1006	0.1024	0.0978	0.1015	0.1065
$^{143}Nd/^{144}Nd$	0.512670	0.512650	0.512699	0.512698	0.512711	0.512725	0.512724	0.512734	0.512733
2σ	10	6	10	10	12	4	6	8	6
$(^{143}Nd/^{144}Nd)_i$	0.51257	0.51256	0.51260	0.51260	0.51261	0.51262	0.51262	0.51263	0.51262
$\varepsilon Nd(t)$	2.6	2.4	3.2	3.2	3.3	3.6	3.7	3.8	3.7
$f_{Sm/Nd}$	−0.51	−0.54	−0.52	−0.52	−0.49	−0.48	−0.5	−0.48	−0.46
T_{DM1} (Ga)	0.63	0.62	0.58	0.58	0.59	0.58	0.56	0.57	0.59
T_{DM2} (Ga)	0.71	0.72	0.66	0.66	0.65	0.64	0.63	0.62	0.63

The notation of $\varepsilon Nd(t)$, $f_{Sm/Nd}$ and T_{DM1} and T_{DM2} are defined as:
$\varepsilon Nd = [(^{143}Nd/^{144}Nd)s/(^{143}Nd/^{144}Nd)_{CHUR} - 1] * 10{,}000$;
$f_{Sm/Nd} = [(^{147}Sm/^{144}Nd)s/(^{147}Sm/^{144}Nd)_{CHUR}] - 1$;
$T_{DM1} = 1/\lambda \ln\{1 + [(^{143}Nd/^{144}Nd)_s - 0.51315]/[(^{147}Sm/^{144}Nd)_s] - 0.2137]\}$;
$T_{DM2} = T_{DM1} - (T_{DM1} - t) * ((f_{cc} - f_s)/(f_{cc} - f_{DM})$;
where S = sample, $(^{143}Nd/^{144}Nd)_{CHUR} = 0.512638$, and $(^{147}Sm/^{144}Nd)_{CHUR} = 0.1967$. λ = decay constants of $^{147}Sm = 0.00654$ Ga. f_{cc}, f_s, f_{DM} are $f_{Sm/Nd}$ values of the continental crust, the sample and depleted mantle, respectively. In our calculation, $f_{cc} = -0.4$, $f_{DM} = 0.0859$ and t = the emplacement age of the granties.

Chappell (1999) and Chappell and White (1992), the aplitic granite and porphyritic granite in the Diyanqinamu drill holes most closely resemble I-type granites because of negative correlation in the P_2O_5 vs. SiO_2 diagram (Fig. 5d, Chappell and White, 1992) and moderate- to slightly peraluminous character (A/CNK <1.1) (Fig. 4b, Chappell, 1999). However, the Sr–Nd isotopic data of the Diyanqinamu granites matched both I-type and A-type classifications. Generally, A-type granites are characterized by alkaline dark mineral content (such as arfvedsonite and riebeckite), enrichment in HFSEs (such as Zr, Nb, Y, and REE), and strong depletion of Ba, Sr, P, Ti, and Eu. The granites in the Diyanqinamu mine contain no mafic alkaline minerals and show no enrichment in Nb or strong depletion of Sr and Eu, which indicates that they are not A-type granites. When plotted on discrimination diagrams (Fig. 9), the Diyanqinamu granite samples all belong to highly fractionated I-type granites.

6.2. Petrogenesis of the granites

Recent studies of Mesozoic voluminous felsic rocks in the northeastern part of China (Hong et al., 2000; Jahn et al., 2000; Wu et al., 2003b) suggest that they were generated mainly from sources containing a large proportion of mantle material (Jahn et al., 2000, 2001). Generally, magma derived directly from the mantle exclusively forms small scale plagiogranites (Shao et al., 2002; Wu et al., 1999). Table 2 suggests that both porphyritic granite and aplitic granite show low $^{87}Rb/^{86}Sr$ radios ($^{87}Rb/^{86}Sr$ <11). Jahn et al. (2000) proposed that granitic rocks with $^{87}Rb/^{86}Sr$ <10 or to 20 could provide a useful constraint to their genetic processes. The granites in the Diyanqinamu mine share the features of low initial $(^{87}Rb/^{86}Sr)_i$ ratios, positive $\varepsilon Nd(t)$ values, and low T_{DM2} model ages with most of these Mesozoic voluminous felsic rocks. However, the Great Xing'an Range is characterized by widely distributed granitic rocks and an absence of coeval/large mafic batholiths, indicating that the Diyanqinamu granites could not be derived directly from the mantle. It should be expected that many melts of mantle derivation have been contaminated by crustal-derived magmas. Jahn et al. (2000) proposed a model of mixed magma sourced from both mantle- and crustally-derived melts, based on positive $\varepsilon Nd(t)$ values and low I_{Sr} ratios. However, isotopic data cannot distinguish between juvenile material from the mantle and juvenile material from mafic lower crust (Topuz et al., 2010), because when the juvenile mafic lower crustal source forms, it is virtually identical in isotopic signature to the mantle at its origin.

Most Phanerozoic granitoids of the CAOB display positive $\varepsilon Nd(t)$ values and young Sm–Nd model ages (mostly 700–800 Ma, Hong

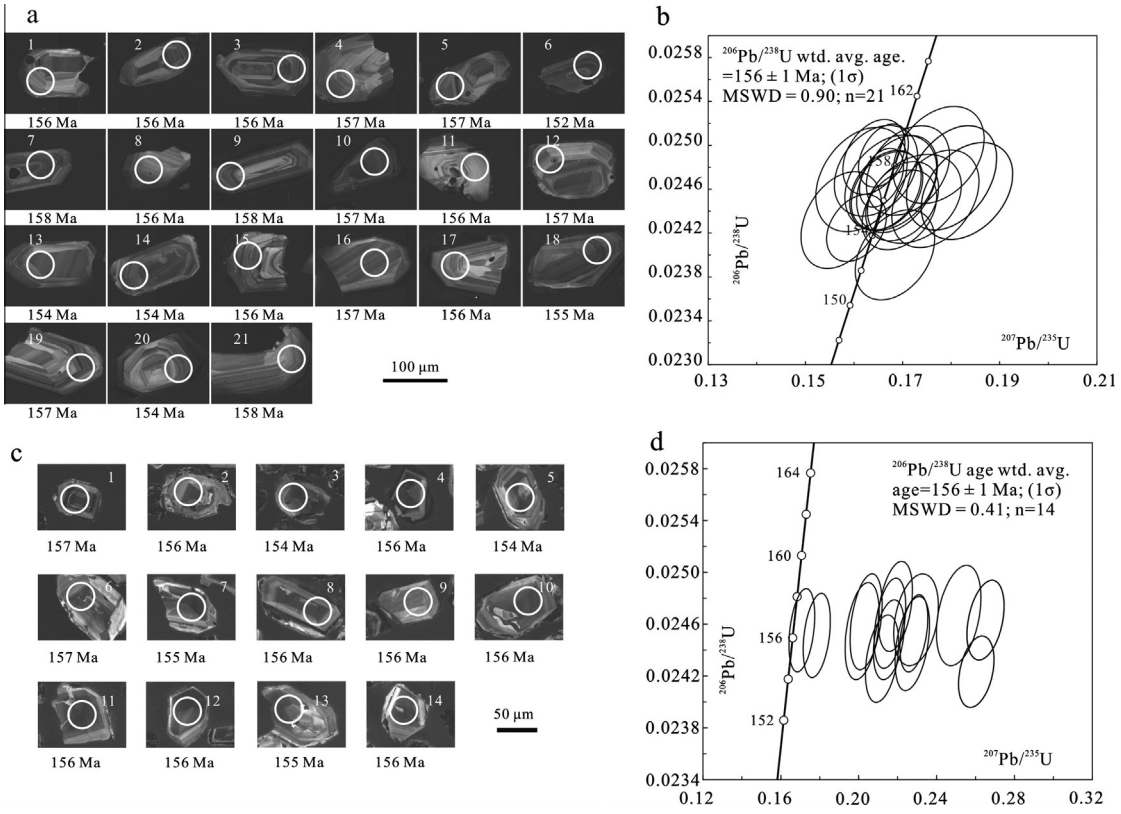

Fig. 7. Cathode Luminescence images of zircons (a, c), and zircon $^{207}Pb/^{235}U$–$^{206}Pb/^{238}U$ concordia plot (b, d) in the Diyanqinamu granites. (a) and (b) show Cathode Luminescence images and concordia plot of the porphyritic granite; (c) and (d) represent Cathode Luminescence images and concordia plot of the aplitic granite.

et al., 2003). The granites in the Diyanqinamu mine also have young Sm–Nd model ages, with a mode of 660 Ma, coeval with peak expansion of the Paleo-Asian Ocean (Dobretsov et al., 1995). Given these correlations with the wide scattered granitoids displaying juvenile crust signature in the CAOB and expansion of the Paleo-Asian Ocean, it is probable that the Diyanqinamu granites were mainly formed by partial melting of both juvenile and "old" pre-existing crustal components (Guo et al., 2010; Hong et al., 2003; Liu et al., 2002; Wu et al., 2002, 2003b).

To estimate the relative proportion of juvenile crust involved in formation of the Diyanqinamu granites, a simple mixing model was applied. Based on a fixed depleted mantle value ($\varepsilon Nd = +8$) and an older crust value ($\varepsilon Nd = -12$) representing the two end-members (Wu et al., 2002), the result of the mixing calculation suggests that the proportion of the juvenile crust at Diyanqinamu varies from 70% to 80% (Fig. 8b). This mixing calculation is consistent across all samples, whether porphyritic or aplitic.

In addition to the matching chemistry and mixing calculations, zircon U–Pb data show that the emplaced ages of the porphyritic granite (156 ± 1 Ma) and the aplitic granite (156 ± 1 Ma) are temporally indistinguishable from each other within error. All plots of these granites show good correlations in Ba vs. Sr (Fig. 10c), δEu vs. SiO_2 (Fig. 10d), and Harker diagrams (Fig. 5), and they share similar Sr and Nd isotopic signatures. These multiple lines of evidence support a genetic relationship between the porphyritic and aplitic granites at Diyanqinamu, and are consistent with a geochemical evolution by fractional crystallization from porphyritic granite to aplitic granite.

The porphyritic granite would represent the relative "parental" magma of the two granites. Fig. 6b shows that the porphyritic granite is strikingly depleted in Ba, Sr, Nb, P, Ti, and Eu, implying that fractional crystallization has occurred. Negative Nb and Ti anomalies are considered related to fractionation of Ti-bearing phases (for example ilmenite and titanite) and negative P anomalies probably result from apatite separation. The Sr, Ba, and Eu depletion require fractionation of plagioclase and/or K-feldspar. The aplitic granite would have formed from the "child" magma, which was the product of fractional crystallization of the "parent" magma. Fig. 10c shows that separation of plagioclase, K-feldspar and, to a lesser extent, biotite occurred during magmatic evolution, as also indicated by the petrography. The observed MgO decrease with increasing SiO_2 suggests the separation of mafic minerals, and petrographic evidence favors a probable fractionation of biotite.

In addition to major phases, the fractionation of accessory minerals seems to have constrained the trace element variation. Both Diyanqinamu granites show constant Nb/Ta ratios (Table 1) with the varying of LOI values, indicating that the alteration process is negligible in disturbing the initial Nb/Ta ratios, and the ratios represent the primary ratios of both granites. The Diyanqinamu granites are characterized by lower Nb/Ta ratios than the value of the continental crust (Green, 1995; Münker, 1998; Taylor and McLennan, 1985) and negative Ti anomalies, which may be attributed to crystallization of Ti-bearing phases (Linnen and Keppler, 1997), such as ilmenite and titanite. In addition, they are characterized by strong depletion in P and very low values of $f_{Sm/Nd}$ (as low as ~−0.54). Their $f_{Sm/Nd}$ values are much lower than that of continental crust ($f_{Sm/Nd}$ = ~−0.4; e.g., Jahn and Condie, 1995), and may be produced by extensive fractional crystallization involving high Sm/Nd accessory minerals, such as apatite and titanite (Wu et al., 2003a). This proposal is also supported by P and Ti anomalies (Fig. 6b) differing markedly between the granites. The decrease in ∑REE from porphyritic granite to aplitic granite implies a separation of minerals with high partition coefficients, e.g., apatite,

Table 3
LA-ICP-MS U–Th–Pb analytical zircon data from the porphyritic granite in drill hole ZK9701 and the aplitic granite in drill hole ZK4522.

Spot no	Pb^c	Th	U	Th/U	Isotopic ratio						Age (Ma)					
	ppm				$^{207}Pb/^{206}Pb$	1σ	$^{207}Pb/^{235}U$	1σ	$^{206}Pb/^{238}U$	1σ	$^{207}Pb/^{206}Pb$	1σ	$^{207}Pb/^{235}U$	1σ	$^{206}Pb/^{238}U$	1σ
Zircons from porphyritic granite																
P-1	6	158	195	0.81	0.0501	0.0017	0.1687	0.0055	0.0246	0.0003	211	78	158	5	157	2
P-2	9	282	282	1	0.0495	0.0015	0.1666	0.0049	0.0246	0.0002	169	70	156	4	157	1
P-3	10	256	348	0.74	0.0508	0.0019	0.1723	0.0064	0.0245	0.0003	232	87	161	6	156	2
P-4	8	192	264	0.73	0.0484	0.0021	0.1614	0.0063	0.0247	0.0003	117	100	152	5	157	2
P-5	13	306	430	0.71	0.0488	0.0019	0.1643	0.0057	0.0248	0.0003	139	89	154	5	158	2
P-6	7	144	241	0.6	0.0527	0.0019	0.1683	0.0054	0.024	0.0003	317	83	158	5	153	2
P-7	12	292	383	0.76	0.0476	0.0013	0.1639	0.0043	0.0249	0.0002	80	63	154	4	159	1
P-8	12	279	411	0.68	0.0504	0.0015	0.1697	0.005	0.0245	0.0002	213	70	159	4	156	2
P-9	5	132	170	0.78	0.0529	0.002	0.1773	0.0062	0.0249	0.0003	324	85	166	5	159	2
P-10	30	492	990	0.5	0.0481	0.0009	0.1655	0.003	0.0247	0.0002	102	44	155	3	157	1
P-11	5	124	179	0.69	0.0556	0.0021	0.1832	0.0063	0.0246	0.0003	435	83	171	5	157	2
P-12	5	123	178	0.69	0.0502	0.002	0.1674	0.0063	0.0247	0.0003	211	95	157	5	157	2
P-13	7	189	246	0.77	0.0478	0.0019	0.1571	0.0055	0.0243	0.0003	100	89	148	5	155	2
P-14	13	279	434	0.64	0.0479	0.0013	0.1603	0.0041	0.0242	0.0002	100	63	151	4	154	1
P-15	7	243	210	1.15	0.0532	0.0019	0.1766	0.006	0.0245	0.0003	339	81	165	5	156	2
P-16	5	109	159	0.69	0.054	0.002	0.18	0.0062	0.0247	0.0003	369	83	168	5	157	2
P-17	13	291	464	0.63	0.049	0.0015	0.1663	0.0049	0.0246	0.0002	146	70	156	4	157	2
P-18	10	221	332	0.67	0.051	0.0017	0.1692	0.0051	0.0244	0.0002	243	76	159	4	155	2
P-19	7	187	203	0.92	0.0513	0.0019	0.171	0.0057	0.0248	0.0003	257	88	160	5	158	2
P-20	9	210	323	0.65	0.0548	0.0016	0.1819	0.0049	0.0243	0.0002	467	69	170	4	155	1
P-21	27	450	914	0.49	0.0478	0.001	0.1659	0.0034	0.0249	0.0002	100	50	156	3	159	1
Zircons from aplitic granite																
A-1	43	1647	1143	1.44	0.0638	0.0017	0.2186	0.0056	0.0247	0.0002	744	57	201	5	158	1
A-2	18	489	580	0.84	0.0673	0.0023	0.2291	0.0074	0.0246	0.0002	848	70	209	6	157	1
A-3	34	1021	1067	0.96	0.077	0.0019	0.2593	0.0059	0.0242	0.0002	1124	48	234	5	154	1
A-4	34	1136	1013	1.12	0.0769	0.0019	0.264	0.0062	0.0246	0.0002	1120	49	238	5	157	1
A-5	27	837	820	1.02	0.0628	0.0017	0.2119	0.0055	0.0243	0.0002	702	62	195	5	155	1
A-6	18	400	550	0.73	0.0731	0.0021	0.2504	0.0074	0.0247	0.0003	1018	55	227	6	157	2
A-7	37	1090	1014	1.08	0.0668	0.0018	0.2271	0.0056	0.0244	0.0002	831	56	208	5	156	2
A-8	24	600	749	0.8	0.0593	0.0017	0.2017	0.0057	0.0245	0.0002	589	60	187	5	156	2
A-9	19	546	587	0.93	0.0636	0.0017	0.2159	0.0053	0.0246	0.0002	728	56	199	4	157	1
A-10	22	570	698	0.82	0.0503	0.0013	0.1713	0.0043	0.0245	0.0002	209	94	161	4	156	1
A-11	30	967	885	1.09	0.0528	0.0014	0.1789	0.0045	0.0245	0.0002	320	66	167	4	156	1
A-12	36	1047	1007	1.04	0.0595	0.0017	0.2037	0.0054	0.0246	0.0002	587	66	188	5	157	2
A-13	29	732	872	0.84	0.0632	0.0016	0.2153	0.0051	0.0245	0.0002	717	53	198	4	156	1
A-14	30	912	829	1.1	0.0667	0.0014	0.228	0.0047	0.0245	0.0002	828	44	209	4	156	1

Pb^c, common lead.

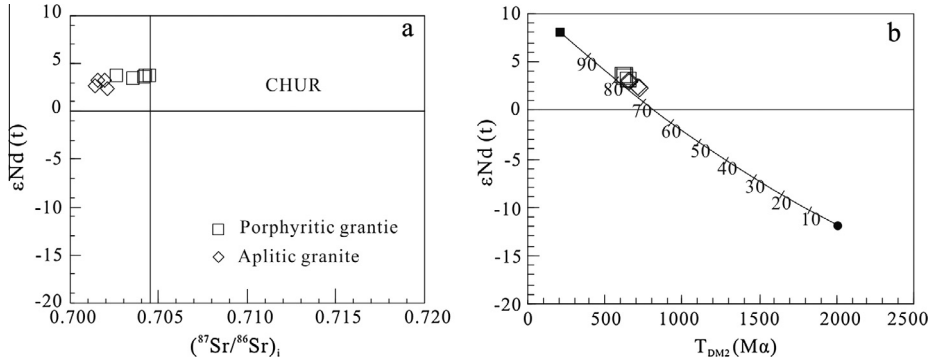

Fig. 8. (a) εNd(*t*) vs. $(^{87}Sr/^{86}Sr)_i$ and (b) εNd(*t*) vs. T_{DM2} diagram showing a linear array and young model ages for porphyritic granite and aplitic granite from the Diyanqinamu mine. The end-member in the diagram is adopted from Wu et al. (2003b).

titanite, zircon, allanite, and monazite. Fig. 10a shows that the variation of REE content appears to be controlled by the fractionation of allanite, monazite, and apatite. However, the negative correlation between P_2O_5 and Th (Fig. 10b) indicates that it follows separation of allanite + apatite instead of monazite during this differentiation process. Their separation would enhance the skewness of the concavity toward HREE and also decrease the overall REE abundance (Wu et al., 2003a), which is consistent with both the HREE signature for these granites and the fluctuation in SiO_2–δEu (Fig. 10d). However, the $(La/Yb)_N$ decrease with reduction of Zr implies that zircon had little influence on REE fluctuation in these granites.

In summary, magmatic evolution of the granites in Diyanqinamu can be explained in terms of a two-stage process: (1) formation of parental magma by melting of a juvenile crust with little contamination from old continental crust, and (2) extensive magmatic differentiation (fractional crystallization) of the parental magma. During the fractional crystallization, Ti-bearing phases, apatite and plagioclase were early products. Later, the fractionation of feldspars, apatite, allanite, ilmenite, and biotite played an important role in forming the aplitic granite from the porphyritic parent. The fractionation of biotite and feldspars was the main cause for the variation in major elements and Rb, Sr, and Ba. The variation of REE was mainly restricted by fractionation of apatite and allanite.

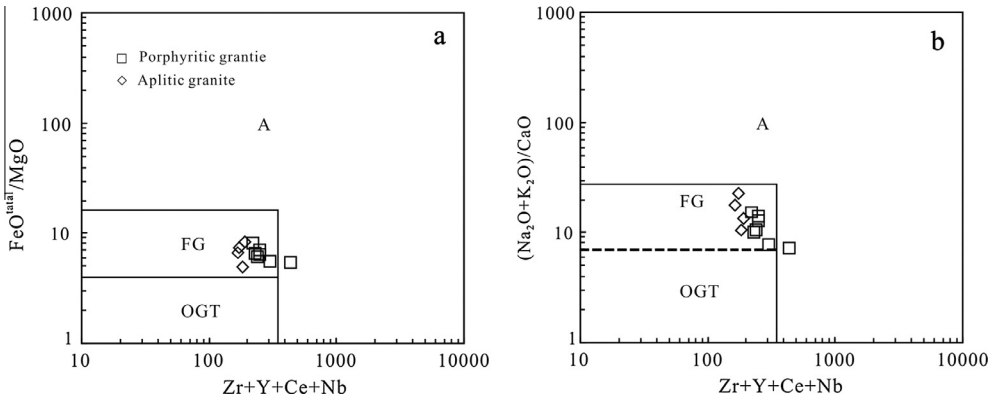

Fig. 9. Discrimination diagrams (a, b) of granites from the Diyanqinamu mine. FG indicates fractionated granite, OGT indicates unfractionated granite, and A indicates A-type granite (Whalen et al., 1987).

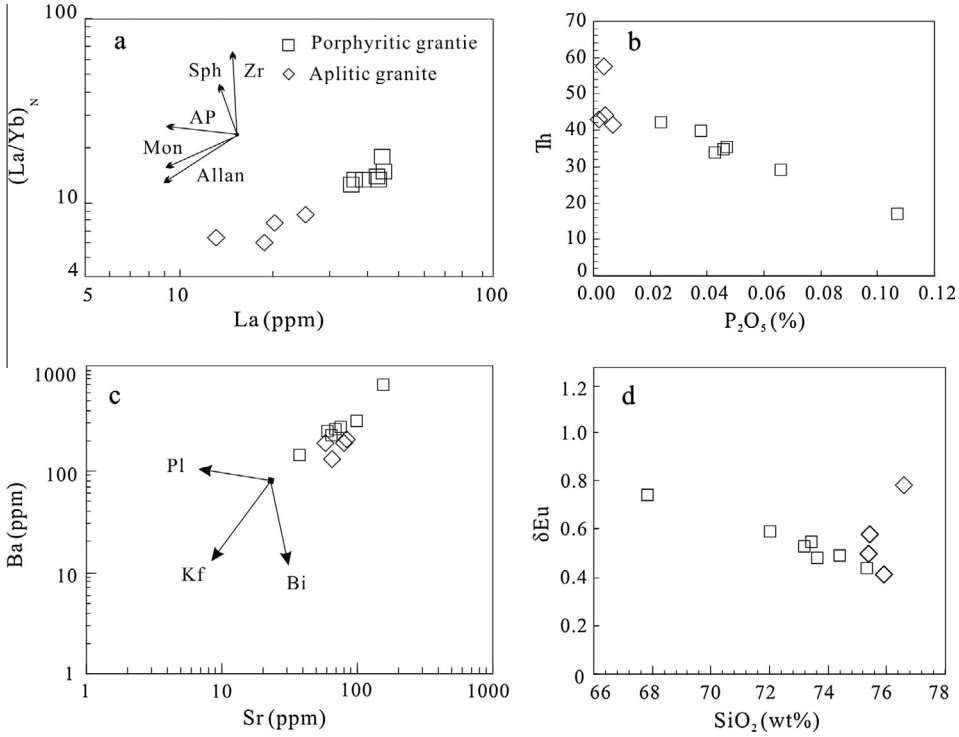

Fig. 10. $(La/Yb)_N$ vs. La diagram (a) showing the change in REE patterns by the separation of accessory minerals, particularly allanite (Allan), apatite (Ap), zircon (Zr), monazite (Mon), and titanite (Sph) (Wu et al., 2003a); P_2O_5 vs. Th diagram (b); Ba vs. Sr diagrams (c) and SiO_2–δEu diagram (d).

6.3. Geodynamic implications

Several proposals have been put forward to explain the driving force for Mesozoic magmatism in the Great Xing'an Range, for example: (1) possible mantle plume activity or certain other intraplate processes (Ge et al., 1999; Lin et al., 1998; Shao et al., 1994, 2001a,b); (2) westward subduction of the Paleo-Pacific plate and related processes such as rifting (Jiang and Quan, 1988; Zhang et al., 2010), asthenospheric upwelling in an extensional backarc setting (Zhang et al., 2011b; Zhao et al., 1989), and delamination (Wang et al., 2006; Zhang et al., 2008b,c, 2010); and, (3) post-orogenic lithospheric extension related to the closure of the Mongol-Okhotsk Ocean (Fan et al., 2003; Meng, 2003; Xu et al., 2013; Ying et al., 2010).

The mantle plume model does not predict the observed scarcity of mantle-derived mafic rocks (such as basalts and gabbros) in the region. Geochronological data demonstrate that this voluminous magmatism lasted for more than 50 Ma in the Great Xing'an Range (Wang et al., 2006), which is far longer than typical short-lived mantle plume volcanism. The linear, rather than clustered, distribution of Mesozoic volcanic rocks in the range also does not support a mantle plume interpretation (Zhang et al., 2011b). In sum, the mantle plume model does not reasonably explain the genesis of the granites in Diyanqinamu.

Subduction of the Paleo-Pacific plate beneath the Eurasian continent is proposed to explain the diminishing trend westward of the Mesozoic volcanism along the whole East Asian continental margin (Wang et al., 2006; Zhang et al., 2008b). The occurrence of a Jurassic–Cretaceous accretionary complex along the East Asian continental margin is also consistent with this interpretation (Isozaki et al., 2010; Utsunomiya et al., 2008; Wu et al., 2007; Zhou et al., 2009). However, paleogenetic data, the eruption of the Paleocene adakitic andesites, and the Tertiary–Quaternary basalts, all indicate that the subduction of the Paleo-Pacific plate only began in Late Cretaceous (Engebretson et al., 1985; Kimura et al., 1990; Maruyama and Send, 1986), but the Diyanqinamu and other

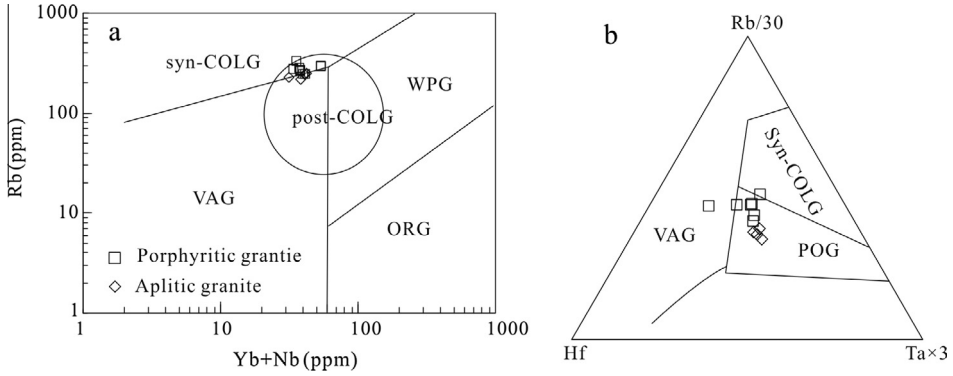

Fig. 11. Tectonic discrimination diagrams of the granites from the Diyanqinamu mine. (a) Rb–Nb + Yb discrimination plots (map based on Pearce (1996)) and (b) Rb–Hf–Ta discrimination diagram (map based on Harris et al. (1986)).

regional granites are Late Jurassic to Early Cretaceous in age. The disparity in timing should be sufficient to dismiss the Paleo-Pacific plate subduction as cause of the magmatism in the Great Xing'an Range. As an additional line of evidence, Xu et al. (2013) also point out that volcanic rocks of Middle–Late Jurassic (155–166 Ma) and Early Cretaceous (138–145 Ma) are only found in the Great Xing'an Range and along the northern margin of the northern China Craton. The lack of coeval volcanic rocks in the Lesser Xing'an and Zhangguangcai ranges and Heilongjiang and Jilin provinces in eastern China, between the Great Xing'an Range and the subduction zone, implies that this volcanism could not be related to the subduction (Xu et al., 2013). Furthermore, the granites in the Diyanqinamu area and Late Jurassic volcanics widespread in eastern Mongolia and Transbaikalia in the central CAOB are far from the subduction belt (Chen et al., 2007; Fan et al., 2003; Wang et al., 2006). Clearly, there is no link between the subduction of the Paleo-Pacific plate and the granites in the Diyanqinamu mine.

The post-orogenic lithospheric extension model related to closure of the Mongol-Okhotsk Ocean is the most feasible explanation for genesis of the granites in Diyanqinamu, based on the timing and distribution of igneous rocks in the region. Zorin (1999) showed that the complete closure of the western part of Mongol-Okhotsk Ocean took place between Early to Middle Jurassic, and Kravchinsky et al. (2002) indicated the eastern section of the Mongol-Okhotsk Orogen formed in Late Jurassic to earliest Cretaceous (Kravchinsky et al., 2002), supporting previous work proposing a scissored west-to-east closing of the ocean basin. During the closure, compressional tectonics were dominant in the central Great Xing'an Range, and lithospheric thickening occurred, such as the Early to Late Mesozoic Yanshanian fold thrust belt and southward-directed thrust nappe structures exposed in northern Inner Mongolia and southern Mongolia (Davis et al., 2001; Meng et al., 2002; Zheng et al., 1998; Zheng and Wang, 2005). However, from the Late Mesozoic, post-orogenic lithospheric extension was dominant in Diyanqinamu and adjacent areas, as evidenced by the occurrence of bimodal volcanic rocks, basin and range tectonics, and a metamorphic core complex (Chen et al., 2009; Davis and Darby, 2010; Graham et al., 2001; Ren et al., 2002; Shao et al., 1998; Wang et al., 2002, 2006; Zorin, 1999). Extensional basins became widely distributed in areas near Diyanqinamu, such as Erlian, Hailar, Songliao, and the eastern Gobi basin in southeastern Mongolia. The eastern Gobi basin, spanning the border of eastern Mongolia and China, includes in basal sediments a volcanic interlayer with an $^{40}Ar/^{39}Ar$ age of 155 ± 1 Ma (Graham et al., 2001), essentially coeval with the Diyanqinamu granites. Equivalents of the Xinganling Group volcanics in outcrops from West Liaoning are well constrained by $^{40}Ar/^{39}Ar$ and K–Ar ages of 156 Ma (Meng, 2003). Volcanism started in Songliao basin in Late Jurassic based on $^{40}Ar/^{39}Ar$ and K–Ar ages of 157.9 ± 2.7 Ma on basalt in basal sediments (Wang et al., 2002). Wang et al. (2006) and Ying et al. (2010) analyzed numerous geochronological studies of Mesozoic rocks in the area and suggested that the Mesozoic volcanism throughout the Great Xing'an Range commenced in Late Jurassic and formed in an extensional setting. Clearly, the Late Jurassic was a transitional period during which the tectonic environment of the Great Xing'an Range changed from compression to extension.

In the Diyanqinamu mine, the high-K calc-alkaline aplitic and porphyritic granites both were emplaced in Late Jurassic. Barbarin (1999) and Zhang et al. (2011a) regarded high-K calc-alkaline granite as a major constituent of late orogenic to post-collisional magmatism and as an indicator of the process of collapse. In tectonic discrimination diagrams of the Diyanqinamu granites, all plots fall into the superposed region of the syn-collision to post-collision granite (Fig. 11), displaying transitional character. Considering all the above, the most likely dominant driving force for granitic magmatism in Diyanqinamu is post-orogenic lithospheric extension related to closure of the Mongol-Okhotsk Ocean.

7. Conclusions

The present study leads to the following conclusions.

(1) The aplitic granite in the Diyanqinamu mine was formed by the fractional crystallization of porphyritic granite. Both the aplitic and porphyritic granites in the mine are highly fractionated I-type granite and were emplaced at 156 Ma, Late Jurassic.
(2) The Sr–Nd isotopic signatures of these granites indicate that they were formed by partial melting of pre-existent crustal components, both "old" and juvenile.
(3) Lithospheric extension subsequent to closure of the Mongol-Okhotsk Ocean was the major force for the formation of the Diyanqinamu granites. The petrogenesis of these granites indicates that a transitional tectonic setting from compression to extension is an important tectonic component for Great Xing'an Range during the Late Jurassic.

Acknowledgments

Hairui Sun is most grateful to the laboratory staff in State Key Laboratory of Ore Deposit Geochemistry, Institute of Geochemistry, Chinese Academy of Sciences, Guiyang, particularly to XiaoBiao Li, Tao Han, Jing Hu, Guangping Bao and Liang Li for their instruction in chemical separation, mass spectrometry, TIMS and LA-ICP-MS

analyses. In addition, we wish to thank Wei Ding and Jiaxi Zhou for the help during our field investigation and constructive suggestions on the earlier drafts respectively. This study is financially supported by the Chinese National Basic Research 973 Program (2013CB429801).

References

Barbarin, B., 1999. A review of the relationships between granitoid types, their origins and their geodynamic environments. Lithos 46, 605–626.

Chappell, B.W., 1999. Aluminium saturation in I- and S-type granites and the characterization of fractionated haplogranites. Lithos 46, 535–551.

Chappell, B.W., White, A.J.R., 1992. I-type and S-type granites in the Lachlan Fold Belt. Trans. R. Soc. Edinburgh: Earth Sci. 83, 1–26.

Chen, Z.G., Zhang, L.C., Wu, H.Y., Zhou, X.H., Liu, Q., 2009. Ar–Ar age, geochemistry and petrogenesis of Late Mesozoic volcanic rocks in the northern marginal region of Erlian basin, Inner-Mongolia. Acta Petrol. Sin. 25, 297–310.

Chen, Y.J., Chen, H.Y., Zaw, K., Pirajno, F., Zhang, Z.J., 2007. Geodynamic settings and tectonic model of skarn gold deposits in China: an overview. Ore Geol. Rev. 31, 139–169.

Davis, G.A., Darby, B.J., 2010. Early Cretaceous overprinting of the Mesozoic Daqing Shan fold-and-thrust belt by the Hohhot metamorphic core complex, Inner Mongolia, China. Geosci. Front. 1, 1–20.

Davis, G.A., Zheng, Y.D., Wang, C., Darby, B.J., Zhang, C.H., Gehrels, G., 2001. Mesozoic tectonic evolution of the Yanshan fold and thrust belt, with emphasis on Hebei and Liaoning Provinces, northern China. In: Hendrix, M.S., Davies, G.A. (Eds.), Paleozoic and Mesozoic Tectonic Evolution of Central Asia: From Continental Assembly to Intracontinental Deformation: GSA Memoir 194, pp. 171–198.

Dobretsov, N.L., Berzin, N.A., Buslov, M.M., 1995. Opening and tectonic evolution of the Paleo-Asian Ocean. Int. Geol. Rev. 37, 335–360.

Engebretson, D.C., Cox, A., Gordon, R.G., 1985. Relative motions between oceanic and continental plates in the Pacific basin. Geol. Soc. Am. Spec. Pap. 206, 1–59.

Fan, W.M., Guo, F., Wang, Y.J., Lin, G., 2003. Late Mesozoic calc-alkaline volcanism of post-orogenic extension in the northern Da Hinggan Mountains, Northeastern China. J. Volcanol. Geotherm. Res. 121, 115–135.

Ge, W.C., Lin, Q., Sun, D.Y., Wu, F.Y., Won, C.K., Lee, M.W., Jin, M.S., Yun, S.H., 1999. Geochemical characteristics of the Mesozoic basalts in Da Hinggan Ling: evidence of the mantle-crust interaction. Acta Petrol. Sin. 15, 397–407 (in Chinese with English abstract).

Graham, S.A., Hendrix, M.S., Johnson, C.L., Badamgarav, D., Badarch, G., Amory, J., Porter, M., Barsbold, R., Webb, L.E., Hacker, B.R., 2001. Sedimentary record and tectonic implications of Mesozoic rifting in southeast Mongolia. Geol. Soc. Am. Bull. 113, 1560–1579.

Green, T.H., 1995. Significance of Nb/Ta as an indicator of geochemical processes in the crust-mantle system. Chem. Geol. 120, 347–359.

Gou, J., Sun, D.Y., Liu, Y.J., Ren, Y.S., Zhao, Z.H., Liu, X.M., 2013. Geochronology, petrogenesis, and tectonic setting of Mesozoic volcanic rocks, southern Manzhouli area, Inner Mongolia. Int. Geol. Rev. 55, 1029–1048.

Guo, F., Fan, W., Gao, X., Li, C., Miao, L., Zhao, L., Li, H., 2010. Sr–Nd–Pb isotope mapping of Mesozoic igneous rocks in NE China: constraints on tectonic framework and Phanerozoic crustal growth. Lithos 120, 563–578.

Harris, N.B.W., Marzouki, F.M.H., Ali, S., 1986. The Jabel Sayid complex, Arabian shield: geochemical constraints on the origin of peralkaline and related granites. J. Geol. Soc., London 143, 287–295.

Hong, D.W., Wang, S., Xie, X.L., Zhang, J.S., 2000. Genesisi of positive $\varepsilon Nd(t)$ grantoids in the Da Hingan MTS.-Mongolia orogenic belt and growth continental crust. Earth Sci. Front. 7, 441–456 (in Chinese with English abstract).

Hong, D.W., Wang, S.G., Xie, L.X., Zhang, J.S., Wang, T., 2003. Metallogenic province derived from mantle source: a case study of Central Asian Orogenic Belt. Miner. Deposits 22, 41–45 (in Chinese with English abstract).

Hu, Z.C., Liu, Y.S., Chen, L., Zhou, L., Li, M., Zong, K.Q., Zhu, L.Y., Gao, S., 2011. Contrasting matrix induced elemental fractionation in NIST SRM and rock glasses during laser ablation ICP-MS analysis at high spatial resolution. J. Anal. At. Spectrom. 26, 425–430.

Isozaki, Y., Aoki, K., Nakama, T., Yanai, S., 2010. New insight into a subduction-related orogen: a reappraisal of the geotectonic framework and evolution of the Japanese Islands. Gondwana Res. 18, 82–105.

Jahn, B.M., Capdevila, R., Liu, D.Y., Vernon, A., Badarch, G., 2004. Sources of Phanerozoic granitoids in the transect Bayanhongor-Ulaan Baatar, Mongolia: geochemical and Nd isotopic evidence, and implications for Phanerozoic crustal growth. J. Asian Earth Sci. 23, 629–653.

Jahn, B.M., Condie, K.C., 1995. Evolution of the Kaapvaal Craton as viewed from geochemical and Sm–Nd isotopic analyses of intracratonic pelites. Geochim. Cosmochim. Acta 59, 2239–2258.

Jahn, B.M., Wu, F.Y., Chen, B., 2000. Granitoids of the Central Asian Orogenic Belt and continental growth in the Phanerozoic. Trans. R. Soc. Edinburgh: Earth Sci. 91, 181–193.

Jahn, B.M., Wu, F.Y., Capdevila, R., Fourcade, S., Wang, Y., Zhao, Z.H., Wang, Y.X., 2001. Highly evolved juvenile granites with tetrad REE patterns: the Woduhe and Baerzhe granites from the Great Xing'an (Khingan) Mountains in NE China. Lithos 59, 171–198.

Jiang, G.Y., Quan, H., 1988. Mesozoic volcanic rocks of Genhe and Hailar basins in Da Hinggan Ling Range. Bulletin of Shenyang Institute Research, Chinese Academy of Geological Science 17, 23–100 (in Chinese with English abstract).

Kimura, G., Takahashi, M., Kono, M., 1990. Mesozoic collision–extrusion tectonics in eastern Asia. Tectonophysics 181, 15–23.

Kravchinsky, V.A., Sorokin, A.A., Courtillot, V., 2002. Paleomagnetism of Paleozoic and Mesozoic sediments from the southern margin of Mongol-Okhotsk Ocean, far eastern Russia. J. Geophys. Res. 107, 2253.

Liew, T.C., Hofmann, A.W., 1988. Precambrian crustal components, plutonic associations, plate environment of the Hercynian Fold Belt of Central Europe: indications from a Nd and Sr isotopic study. Contrib. Miner. Petrol. 98, 129–138.

Lin, Q., Ge, W.C., Sun, D.Y., Wu, F.Y., Won, C.K., Min, K.D., Jin, M.S., Lee, M.W., Kwon, C.S., Yun, S.H., 1998. Tectonic implications of Mesozoic volcanic rocks in Northeastern China. Sci. Geol. Sin. 33, 129–139 (in Chinese with English abstract).

Lin, Q., Ge, W.C., Sun, D.Y., Wu, F.Y., 1999. Geomechanical significance of the Mesozoic volcanics in Northeast Asia. Chin. J. Geophys. – Chinese Edition 42, 75–84.

Linnen, Keppler, 1997. Columbite solubility in granitic melts: consequences for the enrichment and fractionation of Nb and Ta in the Earth's crust. Contrib. Miner. Petrol. 128, 213–227.

Liu, C., Deng, J.F., Xu, L.Q., Zhang, H.D., Kong, W.Q., Li, N., Luo, Z.H., Bai, L.B., Zhao, G.C., Su, S.G., 2011. A preliminary frame of magma-tectonic Mo metallogenic events of Mesozoic Era in Da Hinggan Mountains and Xiao Hinggan Mountains areas. Earth Sci. Front. 18, 166–178 (in Chinese with English abstract).

Liu, Y.S., Hu, Z.C., Zong, K.Q., Gao, C.G., Gao, S., Xu, J., Chen, H.L., 2010a. Reappraisement and refinement of zircon U–Pb isotope and trace element analyses by LA-ICP-MS. Chin. Sci. Bull. 55, 1535–1546 (in Chinese).

Liu, Y.S., Gao, S., Hu, Z.C., Gao, C.G., Zong, K.Q., Wang, D.B., 2010b. Continental and oceanic crust recycling-induced melt-peridotite interactions in the Trans-North China Orogen: U–Pb dating, Hf isotopes and trace elements in zircons from mantle xenoliths. J. Petrol. 51, 537–571.

Liu, H.T., Zhai, M.G., Liu, J.M., Sun, S.H., 2002. The Mesozoic granitoids in the northern marginal region of North China Craton: evolution from post-collisional to an orogenic settings. Acta Perol. Sin. 18, 433–448 (in Chinese with English abstract).

Maruyama, S., Send, T., 1986. Orogeny and relative plate motions: example of the Japanese Islands. Tectonophysics 127, 305–329.

Meng, Q.R., 2003. What drove Late Mesozoic extension of the northern China–Mongolia tract? Tectonophysics 369, 155–174.

Metelkin, D.V., Gordienko, I.V., Klimuk, V.S., 2007. Paleomagnetism of Upper Jurassic basalts from Transbaikalia: new data on the time of closure of the Mongol-Okhotsk Ocean and Mesozoic intraplate tectonics of Central Asia. Russ. Geol. Geophys. 48, 825–834.

Meng, Q.R., Hu, J.M., Yuan, X.J., Jin, J.Q., 2002. Structure, evolution and origin of Late Mesozoic extensional basins in the China–Mongolia border region. Geol. Bull. China 21, 224–231 (in Chinese with English abstract).

Metelkin, D.V., Vernikovsky, V.A., Kazansky, A.Y., Wingate, M.T.D., 2010. Late Mesozoic tectonics of Central Asia based on paleomagnetic evidence. Gondwana Res. 18, 400–419.

Münker, C., 1998. Nb/Ta fractionation in a Cambrian arc back arc system, New Zealand: source constraints and application of refined ICPMS techniques. Chem. Geol. 144, 23–45.

Nie, F.J., Hu, P., Jiang, S.H., Liu, Y.F., 2010. Geologibal features, geochronology and origin of Tungsten and Tungsten (Molybdenum) deposits in the Shamai-Yuguzer mineralization concentrated camp along the Sino-Mongolian border. Acta Geosci. Sin. 31, 383–394 (in Chinese with English abstract).

Nie, F.J., Jiang, S.H., Zhang, Y., Liu, Y., Hu, P., 2004. Geological features and origin of porphyry copper deposits in China–Mongolia border region and its neighboring area. Miner. Deposits 23, 176–189 (in Chinese with English abstract).

Pearce, J.A., 1996. Sources and settings of granitic rocks. Episodes 19, 120–125.

Pitcher, W.S., 1982. Granite type and tectonic environment. In: Hsu, K.J. (Ed.), Mountain Building Processes. Academic Press, London, pp. 19–40.

Pitcher, W.S., 1993. The Nature and Origin of Granite Blackie. Academic and Professional, London (311 pp).

Qi, L., Grégoire, D.C., 2000. Determination of trace elements in twenty-six Chinese geochemistry reference materials by inductively coupled plasma mass spectrometry. Geostandards Newslett. 24, 51–63.

Ren, J., Tamaki, K., Li, S., Junxia, Z., 2002. Late Mesozoic and Cenozoic rifting and its dynamic setting in Eastern China and adjacent areas. Tectonophysics 344, 175–205.

Sengör, A.M.C., Natal'in, B.A., Burtman, V.S., 1993. Evolution of the Altaid tectonic collage and Palaeozoic crustal growth in Eurasia. Nature 364, 299–307.

Sengör, A.M.C., Natal'in, B.A., 1996. Paleotectonics of Asia: fragments of a synthesis. In: Yin, A., Harrison, M. (Eds.), The Tectonic Evolution of Asia. Cambridge University Press, pp. 486–640.

Shao, J.A., Hong, D.W., Zhang, L.Q., 2002. Genesis of Sr–Nd isotopic characteristics of igneous rocks in Inner Mongolia. Geol. Bull. China 21, 818–822.

Shao, J.A., Li, X.H., Zhang, L.Q., Mu, B.L., Liu, Y.L., 2001a. Geochemical conditions for genetic mechanism of the Mesozoic bimodal dyke swarms in Nankou-Guyaju. Geochemica 30, 517–524 (in Chinese with English Abstract).

Shao, J.A., Liu, F.T., Chen, H., Han, Q.J., 2001b. Relationship between Mesozoic Magmatism and Subduction in the Da Hinggan-Yanshan Area. Acta Geol. Sin. – English Edition 75, 1–9.

Shao, J.A., Zang, S.X., Mou, B.L., 1994. Extensional tectonics and asthenospheric upwelling in the orogenic belt: a case study from Hinggan–Mongolia Orogenic belt. Chin. Sci. Bull. 39, 533–537.
Shao, J.A., Zhang, L.Q., Mou, B.L., 1998. Thermo-tectonic evolution in middle and south part of Dahinggan. Sci. China, Ser. D 28, 194–200 (in Chinese).
Sun, S., McDonough, W.F., 1989. Chemical and isotopic systematics of oceanic basalts: implications for mantle composition and processes. In: Saunders, A.D., Norry, M.J. (Eds.), Magmatism in the Ocean Basins. Geological Society, London, Special Publication 42, pp. 313–345.
Sylvester, P.J., 1989. Post-collisional alkaline granites. J. Geol., 261–280.
Taylor, S.R., McLennan, S.M., 1985. The Continental Crust: Its Composition and Evolution. Blackwell, Oxford.
Tomurtogoo, O., Windley, B.F., Kroner, A., Badarch, G., Liu, D.Y., 2005. Zircon age and occurrence of the Adaatsag ophiolite and Muron shear zone, central Mongolia: constraints on the evolution of the Mongol-Okhotsk Ocean, suture and orogen. J. Geol. Soc. 162, 125–134.
Topuz, G., Altherr, R., Siebel, W., Schwarz, W.H., Zack, T., Hasozbek, A., Barth, M., Satir, M., Sen, C., 2010. Carboniferous high-potassium I-type granitoid magmatism in the Eastern Pontides: the Gumushane pluton (NE Turkey). Lithos 116, 92–110.
Utsunomiya, A., Suzuki, N., Ota, T., 2008. Preserved paleo-oceanic plateaus in accretionary complexes: implications for the contributions of the Pacific superplume to global environmental change. Gondwana Res. 14, 115–125.
Wang, P., Liu, W., Wang, S., Song, W., 2002. $^{40}Ar/^{39}Ar$ and K/Ar dating on the volcanic rocks in the Songliao basin, NE China: constraints on stratigraphy and basin dynamics. Int. J. Earth Sci. 91, 331–340.
Wang, F., Zhou, X.H., Zhang, L.C., Ying, J.F., Zhang, Y.T., Wu, F.Y., Zhu, R.X., 2006. Late Mesozoic volcanism in the Great Xing'an Range (NE China): timing and implications for the dynamic setting of NE Asia. Earth Planet. Sci. Lett. 251, 179–198.
Whalen, J.B., Currie, K.L., Chappell, B.W., 1987. A-type granites: geochemical characteristics, discrimination and petrogenesis. Contrib. Mineral. Petrol. 95, 407–419.
Wu, F.Y., Jahn, B.M., Wilde, S., Sun, D.Y., 2000. Phanerozoic crustal growth: U–Pb and Sr–Nd isotopic evidence from the granites in northeastern China. Tectonophysics 328, 89–113.
Wu, F.Y., Jahn, B.M., Wilde, S.A., Lo, C.H., Yui, T.F., Lin, Q., Ge, W.C., Sun, D.Y., 2003a. Highly fractionated I-type granites in NE China (I): geochronology and petrogenesis. Lithos 66, 241–273.
Wu, F.Y., Jahn, B.M., Wilde, S.A., Lo, C.H., Yui, T.F., Lin, Q., Ge, W.C., Sun, D.Y., 2003b. Highly fractionated I-type granites in NE China (II): isotopic geochemistry and implications for crustal growth in the Phanerozoic. Lithos 67, 191–204.
Wu, F.Y., Lin, J.Q., Wilde, S.A., Zhang, X.O., Yang, J.H., 2005. Nature and significance of the Early Cretaceous giant igneous event in eastern China. Earth Planet Sci. Lett. 233, 103–119.
Wu, F.Y., Sun, D.Y., Lin, Q., 1999. Petrogenesis of the Phanerozoic granites and crustal growth in Northeast China. Acta Petrol. Sin. 15, 181–189.
Wu, F.Y., Sun, D.Y., Li, H., Jahn, B.M., Wilde, S., 2002. A-type granites in northeastern China: age and geochemical constraints on their petrogenesis. Chem. Geol. 187, 143–173.
Wu, F.Y., Sun, D.Y., Ge, W.C., Zhang, Y.B., Grant, M.L., Wilde, S.A., Jahn, B.M., 2011. Geochronology of the Phanerozoic granitoids in northeastern China. J. Asian Earth Sci. 41, 1–30.
Wu, F.Y., Wilde, S., Sun, D.Y., 2001. Zircon SHRIMP U–Pb ages of gneissic granites in Jiamusi massif, northeastern China. Acta Petrol. Sin. 17, 443–452 (in Chinese with English abstract).
Wu, F.Y., Yang, J.H., Lo, C.H., Wilde, S.A., Sun, D.Y., Jahn, B.M., 2007. Jiamusi Massif in China: a Jurassic accretionary complex in the western Pacific margin. Island Arc 16, 156–172.
Xue, H.M., Guo, L.J., Hou, Z.Q., Zhou, X.W., Tong, Y., Pan, X.F., 2009. The Xilingele complex from the eastern part of the Central Asian Orogenic Belt, China: products of early Variscan orogeny other than ancient block: evidence from zircon SHRIMP U–Pb ages. Acta Petrol. Sin. 25, 2001–2010.
Xu, C., Huang, Z.L., Qi, L., Fu, P.Q., Liu, C.Q., Li, E.D., Guan, T., 2007. Geochemistry of Cretaceous granites from Mianning in the Panxi region, Sichuan Province, southwestern China: implications for their generation. J. Asian Earth Sci. 29, 737–750.
Xu, W.L., Pei, F.P., Wang, F., Meng, E., Ji, W.Q., Yang, D.B., Wang, W., 2013. Spatial–temporal relationships of Mesozoic volcanic rocks in NE China: constraints on tectonic overprinting and transformations between multiple tectonic regimes. J. Asian Earth Sci. 74, 167–193.
Ying, J.F., Zhou, X.H., Zhang, L.C., Wang, F., 2010. Geochronological framework of Mesozoic volcanic rocks in the Great Xing'an Range, NE China, and their geodynamic implications. J. Asian Earth Sci. 39, 786–793.
Zhang, W.Y., 2008. Magmatic Activity and Metallogeny of Dong Ujimqin Banner, Inner Mongolia. Beijing Chinese Academy of Geological Science (in Chinese with English abstract).
Zhang, F.Q., Chen, H.L., Yu, X., Dong, C.W., Yang, S.F., Pang, Y.M., Batt, G.E., 2011b. Early Cretaceous volcanism in the northern Songliao Basin, NE China, and its geodynamic implication. Gondwana Res. 19, 163–176.
Zhang, J.H., Gao, S., Ge, W.C., Wu, F.Y., Yang, J.H., Wilde, S.A., Li, M., 2010. Geochronology of the Mesozoic volcanic rocks in the Great Xing'an Range, northeastern China: implications for subduction-induced delamination. Chem. Geol. 276, 144–165.
Zhang, J.H., Ge, W.C., Wu, F.Y., Wilde, S.A., Yang, J.H., Liu, X.M., 2008a. Large-scale Early Cretaceous volcanic events in the northern Great Xing'an Range, Northeastern China. Lithos 102, 138–157.
Zhang, W.Y., Nie, F.J., Liu, Y., Jiang, S.H., Xu, D.Q., Guo, L.J., 2008b. $^{40}Ar/^{39}Ar$ geochronology of the aououte Cu–Zn deposit in Inner Mongolia and its significance. Acta Geosci. Sin. 29, 592–598 (in Chinese with English abstract).
Zhang, X.H., Wilde, S.A., Zhang, H.F., Zhai, M.G., 2011a. Early Permian high-K calc-alkaline volcanic rocks from NW Inner Mongolia, North China: geochemistry, origin and tectonic implications. J. Geol. Soc. (London) 168, 525–543.
Zhao, G.L., Yang, G.L., Fu, J.Y., Wang, Z., Fu, J.Y., Yang, Y.Z., 1989. Mesozoic Volcanic Rocks in Central and Southern Da Hinggan Ling Range. Beijing Science and Technology Publishing House, 1–260 (in Chinese with English abstract).
Zhang, L.C., Zhou, X.M., Ying, J.F., Wang, F., Guo, F., Wan, B., Chen, Z.G., 2008c. Geochemistry and Sr–Nd–Pb–Hf isotopes of Early Cretaceous basalts from the Great Xinggan Range, NE China: implications for their origin and mantle source characteristics. Chem. Geol. 256, 12–23.
Zhao, L., Gao, F.H., Zhang, Y.L., Xu, H.M., Zhang, L.Y., 2013. Zircon U–Pb chronology and its geological implications of Mesozoic volcanic rocks from the Hailaer basin. Acta Petrol. Sin. 29, 864–874.
Zheng, Y.D., Davis, G.A., Wand, C., Darby, B.J., Hua, Y.G., 1998. Major thrust sheet in the Daqing Shan Mountains, Inner Mongolia, China. Sci. China, Ser. D 41, 553–560 (in Chinese with English abstract).
Zheng, Y.F., Wang, T., 2005. Kinematics and dynamics of the Mesozoic orogeny and late-orogenic extensional collapse in the Sino-Mongolian border areas. Sci. China, Ser. D: Earth Sci. 48, 849–862.
Zhou, J.B., Wilde, S.A., Zhang, X.Z., Zhao, G.C., Zheng, C.Q., Wang, Y.J., Zhang, X.H., 2009. The onset of Pacific margin accretion in NE China: evidence from the Heilongjiang high-pressure metamorphic belt. Tectonophysics 478, 230–246.
Zonenshain, L., Kuzmin, M., Natapov, L., 1990. Geology of RSSR: a plate tectonic synthesis. Am. Geophys. Union, Geodyn. Ser. 21, 242.
Zorin, Y.A., 1999. Geodynamics of the western part of the Mongolia-Okhotsk collisional belt, Trans-Baikal region (Russia) and Mongolia. Tectonophysics 306, 33–56.